doi:10.20944/preprints202107.0051.v1

Article

Topology Optimization of Large-Scale 3D Morphing Wingstructures

Peter Dørffer Ladegaard Jensen [1,*], Fengwen Wang [1], Ignazio Dimino [2] and Ole Sigmund [1]

[1] Dept. of Mechanical Engineering, Technical University of Denmark, 2800 Kgs. Lyngby, Denmark
[2] Adaptive Structures Technologies, The Italian Aerospace Research Centre, CIRA, Via Maiorise, 81043 Capua, Italy
* Correspondence: pdlj@mek.dtu.dk

Abstract: This work proposes a systematic topology optimization approach to simultaneously design the morphing functionality and actuation in three-dimensional wing structures. The actuation is assumed to be a linear strain-based expansion in the actuation material and a three-phase material model is employed to represent structural and actuating materials, and void. To ensure both structural stiffness with respect to aerodynamic loading and morphing capabilities, the optimization problem is formulated to minimize structural compliance while morphing functionality is enforced by constraining a morphing error between actual and target wing shape. Moreover, a feature mapping approach is utilized to constrain and simplify actuator geometries. A trailing edge wing section is designed to validate the proposed optimization approach. Numerical results demonstrate that three-dimensional optimized wing sections utilize a more advanced structural layout to enhance structural performance while keeping morphing functionality than two-dimensional wing ribs. The work presents the first step towards systematic design of three-dimensional morphing wing sections.

Keywords: Topology Optimization; Morphing Wing; Aerospace Design Optimization; Smart and Adaptive Structures; Feature Mapping

Citation: Jensen, P. D. L.; Wang, F.; Dimino, I.; Sigmund, O Topology Optimization of Large-Scale 3D Morphing Wingstructures. *Preprints* **2021**, *1*, 0. https://doi.org/

Received:
Accepted:
Published:

1. Introduction

Since the earliest forms of aviation, efforts have been made to minimize drag resulting from discontinuous flight control surfaces. The Wright brothers solved roll control using a wing-warping mechanism in their first flying machine. Other remarkable historical examples are Holle's adaptive systems for modifying leading and trailing edges [1] and Parker's variable camber wing [2] used to increase cruising speed by continuously varying the geometrical wing characteristics by means of a proper arrangement of the internal structure.

Since that time, the idea of creating motion using flexible structures became unreasonable from the viewpoint of engineering design since engineering practice gradually tried to avoid flexibility, and many systems were designed to be rigid. Traditional metals, such as aluminum, stainless, and titanium, dominated the aerospace industry for over fifty years, as they were considered lightweight, inexpensive, and state-of-the-art. Meanwhile, the interest in cost-effective fuel-efficiently aircraft technologies increased gradually, and these metals started ceding territory to new alloys and composite materials designed to offer lighter weight, greater strength, better corrosion resistance, and reduced assembly and manufacturing costs. Once only considered for non-critical interior cabin components, composite materials are now occupying the space of traditional materials for a wide range of aircraft components, including wing, fuselage, landing gear, and engine.

However, a variation of this trend exists even in modern commercial aircraft, as the use of metallic structures has not entirely disappeared. Aircraft mechanisms, predominantly made from metallic components, continue to be developed and improved to offer ever-increasing performance and more effective deployment kinematics. Metallic mechanisms are still used for both the primary and secondary control surfaces and for landing gear deployment and stowage.

However, the design templates of such traditional wings, conceived of rigid structures with discrete control surfaces operated by rigid-body mechanisms, are a century old. They provide the current standard of adaptive wing airfoils, necessary to efficiently meet the stringent aircraft aerodynamic requirements, involving both high-speed efficiency in cruise and high-lift performance in take-off and landing conditions. However, they do no justice to what nature has achieved in birds; in flight, they are capable to actively morph their wings accordingly to produce sufficient lift and thrust and control and stabilize their flight. The simultaneous push for enhanced aircraft flight performance, control authority, and multi-mission capability, and the advent of one-piece designs, reducing the number of components in overall assemblies, have motivated investigations into conformal morphing systems. In this study, a continuous span morphing wing trailing edge is considered, with the goal of increasing aircraft aerodynamic efficiency and reducing assembly time and costs. We define a *morphing wing device* as a structural system with a continuous skin and an internal mechanism capable of achieving morphing of the outer skin.

With the continuous drive to decrease weight, topology optimization [3,4] has been used to design lightweight and adaptive compliant mechanisms [5]. Furthermore, mechanism design is often a complex task based on experience and trial and error approaches. Sigmund [6] proposed using topology optimization to the systematic design of mechanisms, both on a micro- and a macro scale. The systematic design of mechanisms is obtained by optimizing a domain to generate a specific shape. Sigmund [7,8] also extended mechanism design to multiphysical and multi-material models by modeling bi-material electrothemomechanical actuators using topology optimization.

Studies of topology optimization of morphing wing mechanisms are limited to two-dimensional (2D) models. Kambayashi *et al.* [9] presented a method for obtaining a multi-layered compliant mechanism for a morphing wing under multiple flight conditions. Tong *et al.* [10] studied topology optimization of composite material integrated into a compliant mechanism for a morphing trailing edge. Zhang *et al.* [11] presented a study of a morphing wing leading edge driven by a compliant mechanism design. De Gaspari [12] proposed a design of adaptive compliant wing through a multilevel optimization approach where, sizing, shape and topology optimization are adopted. Gomes and Palacios [13] presented a method for a two-step optimization of aerodynamic shape adaptation a compliant mechanism, by modeling fluid-structure interaction problems combining with density-based topology optimization. Gu *et al.* [14] presented a method for finding a optimized structural layout of a morphing wing, and simultaneously finding the layout of a driving actuator, by modeling a Shape Memory Alloy (SMA) wire.

All of the above studies only address the mechanism as a 2D structure, and as the movement of a morphing structure is not necessarily restricted to 2D results might be inferior. Furthermore, a 2D study limits the potential solution space for optimization and does not give much insight, except as an academic example. Hence a superior mechanism design can be obtained if the problem is posed in three-dimensional (3D) space.

The majority of the mechanisms presented in the above studies are driven by an external force or displacement, meaning that in practice, additional space is required for an actuator(s) in the morphing structure, as investigated in [15]. Actuating, as part of the mechanism, could prove a better overall volume optimum for a morphing wing, as seen in [14]. Therefore, this paper proposes a novel approach for simultaneously designing mechanism and actuating for 3D morphing structures via the topology optimization method. A three-phase material interpolation scheme is employed to represent structural and actuating materials, and void in the optimization procedure. In order to conceive a 3D topology optimization method efficiently, a parallel framework is utilized.

The paper is organized as follows: Section 2 introduces the modeling of a morphing wing structure, with a brief description of the finite element formulation; section 3 presents the proposed topology optimization methodology; section 4 shows optimized morphing wing structures for different design domain formulations; and section 5 and 6 provides a discussion and conclusions.

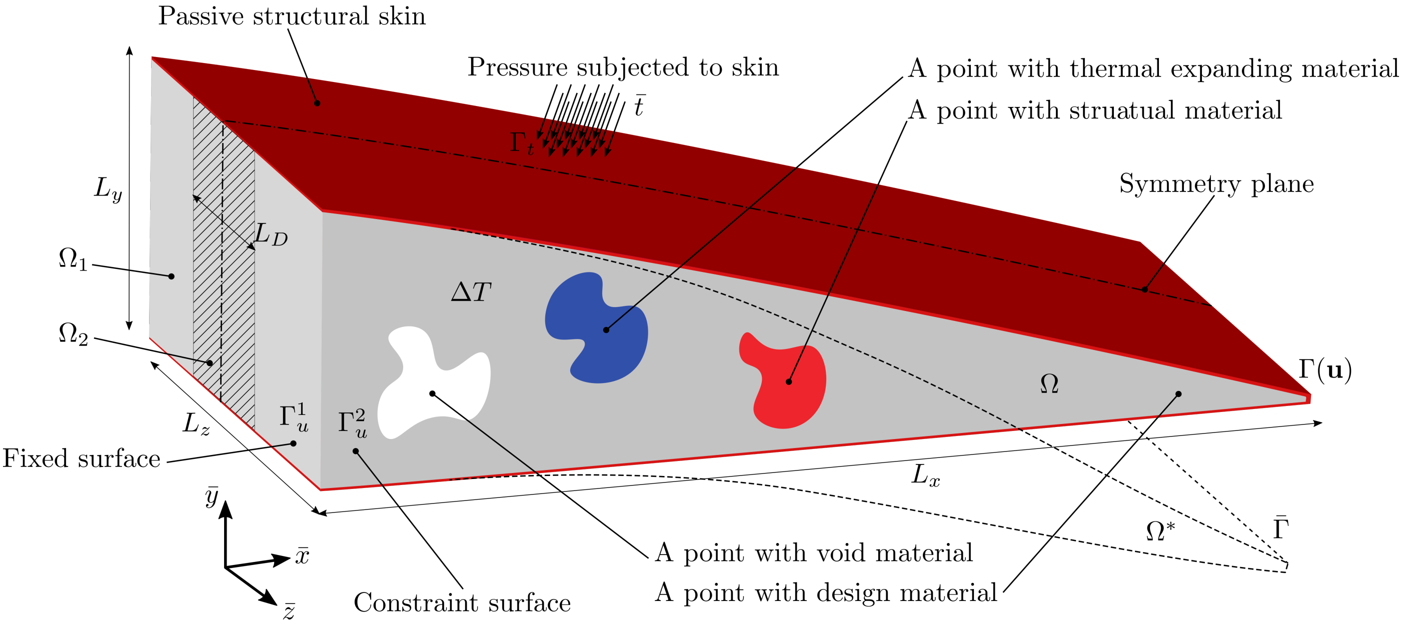

Figure 1. Design problem for morphing trailing edge section.

2. Optimization Model

The optimization problem concerns the composition of void-, structural-, and actuating material in the design domain Ω for a trailing edge wing model, such that the surface $\Gamma(\mathbf{u})$ (function of the state field, $\mathbf{u}$) of the trailing edge, will deform to a target surface $\bar{\Gamma}$ in the morphed domain Ω^*. Simultaneously stored strain energy from a surface traction $\bar{t}$ must be minimized for stiffness maximization. The actuation is assumed to be a linear strain-based expansion in the actuating material, stimulated by a thermal change ΔT. This may also be interpreted as a simple linear model of a SMA based actuator. The problem is illustrated in Fig. 1. Some areas of Ω may be restricted to be passive material, i.e., void, structural, or actuating materials.

The trailing edge model has been inspired by Vecchia *et al.* [16], and is realized as follows. A NACA 2414 airfoil is considered as a base model. The airfoil is illustrated in Fig. 2. We use the software application XFOIL [17] to calculate the aerodynamic load case subjected to the airfoil in the form of pressure coefficients. The pressure is calculated based on an assumed attack of angle of 5°, inviscid flow, and a free stream velocity of $70[\mathrm{m/s}]$ at sea level. For the trailing edge, we only consider the airfoil in the range $x/c = [0.65, 1]$, which is highlighted as the *trailing edge region* in Fig. 2. $c = 1400[\mathrm{mm}]$ is the cord. The trailing edge region has the reference coordinate system $(\bar{x}, \bar{y})$, and the dimension $L_x \times L_y$.

The target morphing shape is obtained by rotating the camber line gradually with morphing angle $\alpha_m = \sin(\bar{x}\pi/(2L_x))\alpha_0$ with $\alpha_0 = -10^\circ$ being the tip morphing angle. The rotation is with respect to the cord line, such that the beginning and end of the target morphing shape experiences little bending, illustrated in Fig. 2.

The 2D airfoil profile, pressure model, and target morphing shape is extruded in the out-of-plane direction $(\bar{z})$ with $L_z = 500[\mathrm{mm}]$, so a wing section is formed, as seen in Fig. 1. The internal part of the trailing edge section (i.e., the design domain) is divided into two sections, where the middle section has the width L_D so that the design domain can be segmented into the sub design domains, Ω_1 (light gray) and Ω_2 (hatched), see Fig. 1. In the following problems $L_D = 0.1L_z$ is used. The design domain of the trailing edge section is enclosed by a skin (passive domain) with a thickness of $2[\mathrm{mm}]$. The trailing edge section is modeled with symmetry $(\bar{x}, \bar{y})$-plane at $0.5L_z$, the surface Γ_u^1 is fixed, and the surface Γ_u^2 is constrained with no $\bar{z}$-displacement (symmetry).

The chosen material properties are listed in Tab. 1. The structural and actuating materi-

doi:10.20944/preprints202107.0051.v1

als are represented by subscripts 1 and 2, respectively. The skin has the same material properties as the structural material. The thermal change is set to unity.

Table 1. Material properties for the trailing edge model.

E_1 [GPa]	E_2 [GPa]	ν_1 $[-]$	ν_2 $[-]$	α_1 $[-]$	α_2 $[-]$
72	70	0.32	0.32	0	0.1

The governing equation for the above problem is given in the standard finite element formulation, for two load cases,

$$\mathbf{K}\mathbf{u}_i = \mathbf{f}_i, \quad i \in \{1, 2\} \tag{1}$$

with $\mathbf{K}$, $\mathbf{u}_i$, and $\mathbf{f}_i$ denoting the global-stiffness matrix, displacement and force vectors, respectively. The domain Ω is discretized by non-regular 8-node tri-linear hexahedral isoparametric elements. $\mathbf{K}$ is assembled from element stiffness matrixes, $\mathbf{K}_e$. For more details on finite element analysis, the reader is referred to [18].
We define the two load cases as

$$\mathbf{f} = \begin{cases} \mathbf{f}_{\text{ext}} + \mathbf{f}_{\text{int}} \\ \mathbf{f}_{\text{ext}} \end{cases}, \tag{2}$$

where the subscript 'ext' and 'int' denotes external and internal loading, respectively. The external loading, is defined as the aerodynamic loading on surface Γ_t. The internal loading is defined as the linear strain-based actuator expansion, modeled as the linear element-volume expansion force. It depends on the element constitutive law, $\mathbf{C}_e$ and the element thermal expansion coefficient α_e and the temperature change ΔT,

$$\mathbf{f}_{e,\text{int}} = \int_{\Omega_e} \mathbf{B}_e^T \, \mathbf{C}_e \, \boldsymbol{\varepsilon}_0 \, \mathrm{d}V_e, \quad \boldsymbol{\varepsilon}_0 = \{\alpha_e, \alpha_e, \alpha_e, 0, 0, 0\}^\top \Delta T, \tag{3}$$

where $\mathbf{B}_e$ denotes the elemental strain-displacement matrix.

3. Topology Optimization

3.1. Optimization Problem

The design problem for a morphing wing structure is sketched in Fig. 1, while an illustration of the target shape is illustrated in the highlight in Fig. 2, as the 2D profile. As stated in the previous section, the morphing functionality is realized by constraining the error between $\Gamma(\mathbf{u})$ and $\bar{\Gamma}$, where $\Gamma(\mathbf{u})$ and $\bar{\Gamma}$ are composed of N degrees of freedom (dof) representing the real and target morphing shapes, respectively. The error is calculated based on the nodal displacement. In Fig. 2 an example is shown for target point i (shown in solid blue on the figure), where the distance d is the nodal displacement change between the original nodal point and morphed target nodal point.
In this work, we use two methods to parameterize the multiple material distribution in the design domain, i.e., a density based approach and a feature mapping based approach. Details of design parameterizations are presented in subsection 3.2. To ensure structural stiffness, we formulate the optimization problem for morphing wings as structural compliance minimization under aerodynamic loading, while the morphing functionality is enforced as a constraint, stated as,

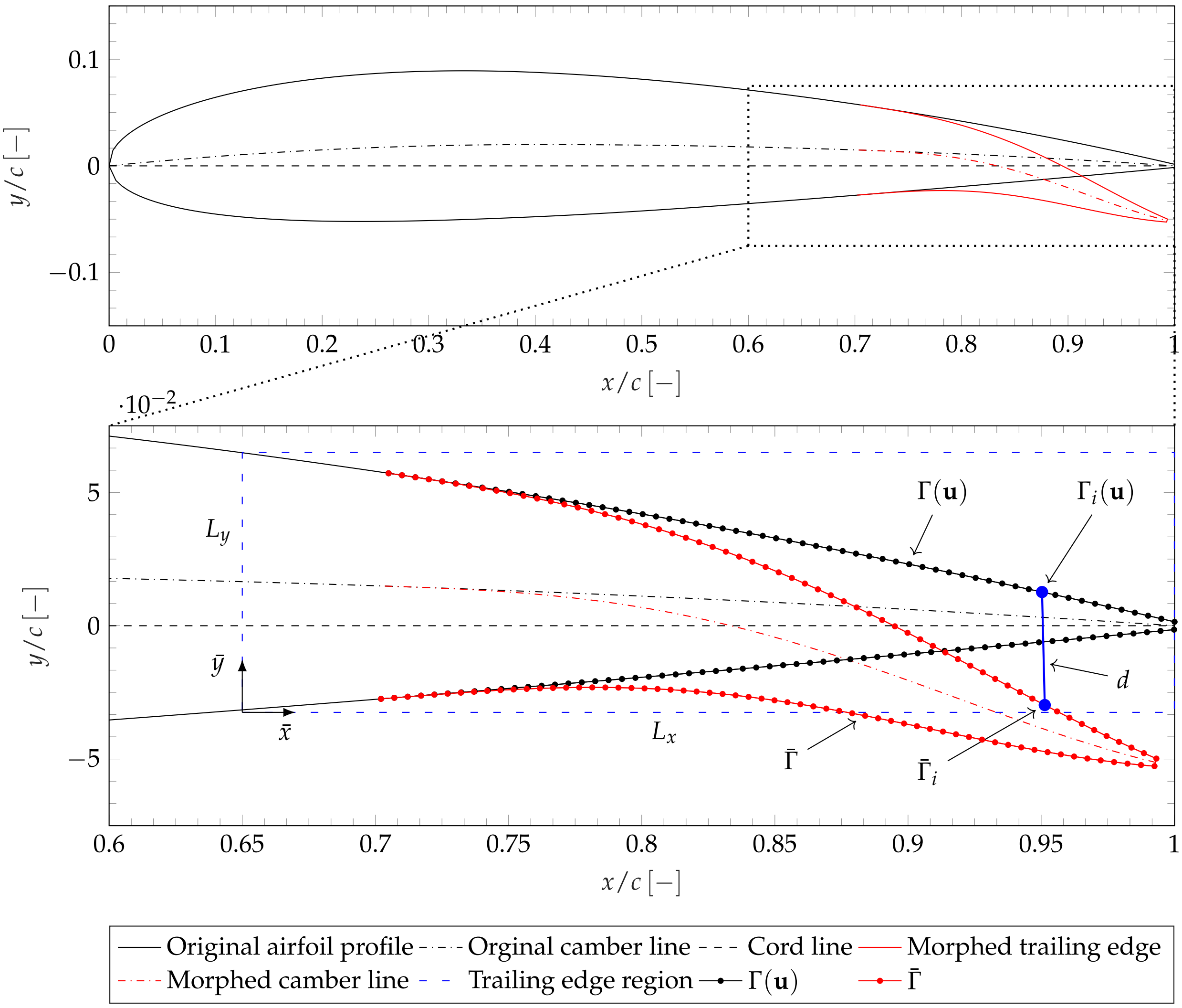

Figure 2. A NACA 2414 2D airfoil profile is illustrated with the morphed trailing edge (red line). $(\bar{x}, \bar{y})$ defines the reference coordinate system for the trailing edge region (blue dashed line), with the dimensions $L_x \times L_y$. The trailing edge section is highlighted, here the nodal points of the original profile, $\Gamma(\mathbf{u})$, and the nodal target points, $\bar{\Gamma}$, are shown. The blue line and dots show the error as the distance, d, for node and target i.

$$\left.\begin{array}{rl} \min\limits_{\boldsymbol{\xi}} & : \quad \mathcal{C}(\boldsymbol{\xi}) = \mathbf{f}_2^\top \mathbf{u}_2 \\ \text{s.t.} & : \quad \mathbf{K}(\boldsymbol{\xi})\mathbf{u}_i = \mathbf{f}_i, \quad i \in \{1,2\} \\ & \quad\;\; \log(\mathcal{E}(\boldsymbol{\xi})/\mathcal{E}^*) \leq 0 \\ & \quad\;\; \mathcal{F}_1(\boldsymbol{\xi}) - \mathcal{F}_1^* \leq 0 \\ & \quad\;\; \mathcal{F}_2(\boldsymbol{\xi}) - \mathcal{F}_2^* \leq 0 \\ & \quad\;\; \mathbf{0} \leq \boldsymbol{\xi} \leq \mathbf{1} \end{array}\right\}, \tag{4}$$

$\mathcal{E}(\boldsymbol{\xi})$ denotes the morphing displacement error between a given target morphing and actual wing shapes, logarithm (log) is employed to normalize the constraint. $\mathcal{F}_1(\boldsymbol{\xi})$ and $\mathcal{F}_2(\boldsymbol{\xi})$ denote the volume fractions of the structural and actuating materials, $\mathcal{E}^*$, $\mathcal{F}_1^*$, and $\mathcal{F}_2^*$, are corresponding prescribed upper bounds.

The displacement error is formulated as the aggregation p-mean function of the relative error of N target degrees of freedom,

$$\mathcal{E}(\boldsymbol{\xi}) = \left(\frac{1}{N}\sum_{i=1}^{N}(\epsilon_i(\mathbf{u}_1))^p\right)^{\frac{1}{p}}, \quad \boldsymbol{\epsilon}(\mathbf{u}_1) = \frac{1}{\max|\bar{\boldsymbol{\Gamma}}|}(\bar{\boldsymbol{\Gamma}} - \boldsymbol{\Gamma}(\mathbf{u}_1)), \tag{5}$$

where $p = 2$ is used. The volume constraints will be defined in the following subsection 3.2 where two design parameterizations are introduced.

3.2. *Density Parameterizations and Interpolation Functions*

Two different design parameterizations are employed in this study, i.e., a density based approach and a feature mapping based approach. In both cases, two element-wise density fields are used to indicate the material occupations.

In order to avoid mesh-dependency and checkerboard pattern [19,20] and enhance the discreteness of designs, we employ a three-field approach as formulated by [21]. A element-wise density field $\mathbf{x}$ is first filtered, $\tilde{\mathbf{x}}$, using the modified Helmholtz-equation type PDE filter [22], stated as

$$-R^2\nabla^2\tilde{\mathbf{x}} + \tilde{\mathbf{x}} = \mathbf{x}, \tag{6}$$

where $R = r_{\text{min}}/\sqrt{12}$ and r_{min} is the physical filter radius. A physical density field $\bar{\tilde{\mathbf{x}}}$ is then obtained by a modified smooth Heaviside function

$$\bar{\tilde{\mathbf{x}}} = \frac{\tanh(\beta\eta) + \tanh(\beta(\tilde{\mathbf{x}} - \eta))}{\tanh(\beta\eta) + \tanh(\beta(1 - \eta))}. \tag{7}$$

Here β controls the steepness/sharpness of the function, and η sets the threshold value.

3.2.1. Density Approach

In the density based approach, denoted *density approach*, we introduce two design variables per element to parameterize the material distributions, i.e., a materiel density design variable ρ_e, and a material phase design variable φ_e with $\rho_e, \varphi_e \in [0, 1]$. Hence, the design variables and two density fields are

$$\boldsymbol{\xi} = \{\boldsymbol{\rho}, \boldsymbol{\varphi}\}^\top, \qquad \mathbf{x} \in \{\boldsymbol{\rho}, \boldsymbol{\varphi}\}^\top. \tag{8}$$

In this approach, $\bar{\tilde{\rho}}_e = 1$ and $\bar{\tilde{\varphi}}_e = 1$ indicate the element is occupied by actuating material, $\bar{\tilde{\rho}}_e = 1$ and $\bar{\tilde{\varphi}}_e = 0$ by structural material, and $\bar{\tilde{\rho}}_e = 0$ by void. Hence, the volume fractions of the structural and actuating materials are calculated by

$$\mathcal{F}_1 = \sum_e \frac{V_e\,\bar{\tilde{\rho}}_e(1 - \bar{\tilde{\varphi}}_e)}{V}, \quad \mathcal{F}_2 = \sum_e \frac{V_e\,\bar{\tilde{\rho}}_e\bar{\tilde{\varphi}}_e}{V}, \tag{9}$$

where V_e is the element volume, and V the total volume of Ω.
We employ the three-phase material model proposed by Sigmund [8] to interpolate the elemental material properties, given as

$$\begin{aligned}
G(\bar{\tilde{\rho}}_e, \bar{\tilde{\varphi}}_e) &= \bar{\tilde{\rho}}^p\,\Phi_G(\bar{\tilde{\varphi}}_e), && (10)\\
K(\bar{\tilde{\rho}}_e, \bar{\tilde{\varphi}}_e) &= \bar{\tilde{\rho}}^p\,\Phi_K(\bar{\tilde{\varphi}}_e), && (11)\\
\alpha(\bar{\tilde{\varphi}}_e) &= \frac{(K_1\,\alpha_1 - K_2\,\alpha_2)K(\bar{\tilde{\varphi}}_e) - K_1\,K_2\,(\alpha_1 - \alpha_2)}{K(\bar{\tilde{\varphi}}_e)(K_1 - K_2)}, && (12)
\end{aligned}$$

with the phase interpolations defined as;

$$\begin{aligned}
\Phi_G(\bar{\tilde{\varphi}}_e) &= (1 - \Psi)G_{\text{L}}^{\text{HSW}}(\bar{\tilde{\varphi}}_e) + \Psi\,G_{\text{U}}^{\text{HSW}}(\bar{\tilde{\varphi}}_e), && (13)\\
\Phi_K(\bar{\tilde{\varphi}}_e) &= (1 - \Psi)K_{\text{L}}^{\text{HS}}(\bar{\tilde{\varphi}}_e) + \Psi\,K_{\text{U}}^{\text{HS}}(\bar{\tilde{\varphi}}_e). && (14)
\end{aligned}$$

Here, $G_{\text{L}}^{\text{HSW}}$ and $G_{\text{U}}^{\text{HSW}}$ are the lower and upper Hashin-Shtrikman-Walpole (HSW) bounds on the shear modulus, and K_{L}^{HS} and K_{U}^{HS} are the lower and upper Hashin-Shtrikman (HS) bounds on the bulk modulus. The bound formulation is shown in the appendix of [8].

$\Psi \in [0,1]$ interpolates linearly between the lower and upper bounds and works as a penalization mechanism for intermediate densities. $K(\bar{\tilde{\varphi}}_e)$ is found from (11) by setting $\bar{\tilde{\rho}} = 1$. The interpolation of the linear strain-based expansion is important as it scales correctly with the material stiffness and hence stays monotonic.

3.2.2. Feature Mapping Approach

Density-based topology optimization often results in rather complex, distributed and very 'natural' looking structures. Simpler geometry representation of the actuating material regions is highly desired from a manufacturing point of view. To impose this while still representing the design domain on a fixed grid, a feature mapping based approach is adopted.

Feature mapping is a broad term which defines the general method for representing or mapping high-level geometric feature parameterization on a fixed non-conforming grid. The first use of feature mapping was demonstrated by Norato *et al.* [23]. The reader is referred to the comprehensive review by Wein *et al.* [24] on feature mapping, for more details.

In this study, geometric features are implicitly represented using a *feature mapped density field*, χ. We use a super-ellipsoid to describe the actuator (similar to Wang [25]), where the center of the super-ellipsoid is located with $\mathbf{r}_0 = \{x_0,\, y_0,\, z_0\}^\top$. For a given element located at $\mathbf{r}_e$, the relation between the element and the super-ellipsoid is represented by

$$H(\boldsymbol{\kappa}) = \left(|a|^{m_{12}} + |b|^{m_{12}}\right) r^{-m_{12}} + |c|^{m_3} l^{-m_3} - 1. \tag{15}$$

Here $H < 0$ indicates that the element is inside of the super-ellipsoid, and $H = 0$ on the boundary, $H > 0$ for outside. $\mathbf{r}_H = \{a,\, b,\, c\}^\top$ are the transformed translational coordinates, defined by:

$$\mathbf{r}_H = \mathbf{r}_e - \mathbf{A}(\theta_1,\, \theta_2)\mathbf{r}_0. \tag{16}$$

$\mathbf{A}$ is a general rotations matrix controlled by the two rotation angles, θ_1 and θ_2. r and l are the semidiameters. The exponents m_{12} and m_3 define the feature approximation of the super-ellipsoid. For $m_{12} = 2$ and $m_3 \to \infty$ the super-ellipsoid will become a cylinder. We use $m_{12} = 2$ and $m_3 = 100$.

The design vector, $\boldsymbol{\kappa}$, of the super-ellipsoid is

$$\boldsymbol{\kappa} = \{x_0,\, y_0,\, z_0, \theta_1,\, \theta_2,\, r,\, l\}, \tag{17}$$

The individual design variables in $\boldsymbol{\kappa}$ are normalized for the optimization problem, here we scale the angles by 8π.

The feature mapped density field χ is generated using a smoothed Heaviside function,

$$\chi(\boldsymbol{\kappa}) = 1 - \frac{1}{1 + \exp(-\beta_2\, H(\boldsymbol{\kappa}))}, \tag{18}$$

where β_2 controls the steepness/sharpness of the function, like the projection filter [21]. With the feature mapped density field, the design domain is now controlled by the element-wise density design variable, $\boldsymbol{\rho}$ and, the feature parameters, $\boldsymbol{\kappa}$, this formulated will be referred to as the *feature mapping approach*.

In this approach, the design vector, $\boldsymbol{\xi}$, and two density fields, are

$$\boldsymbol{\xi} = \{\boldsymbol{\rho}, \boldsymbol{\kappa}\}^\top, \qquad \mathbf{x} \in \{\boldsymbol{\rho}, \chi(\boldsymbol{\kappa})\}^\top. \tag{19}$$

Here, $\bar{\tilde{\chi}}_e = 1$ indicates the element is occupied by actuating material, $\bar{\tilde{\rho}}_e = 1$ and $\bar{\tilde{\chi}}_e = 0$ by structural material, $\bar{\tilde{\rho}}_e = 0$ and $\bar{\tilde{\chi}}_e = 0$ by void. Hence, the volume fractions of the structural and actuating materials are calculated by

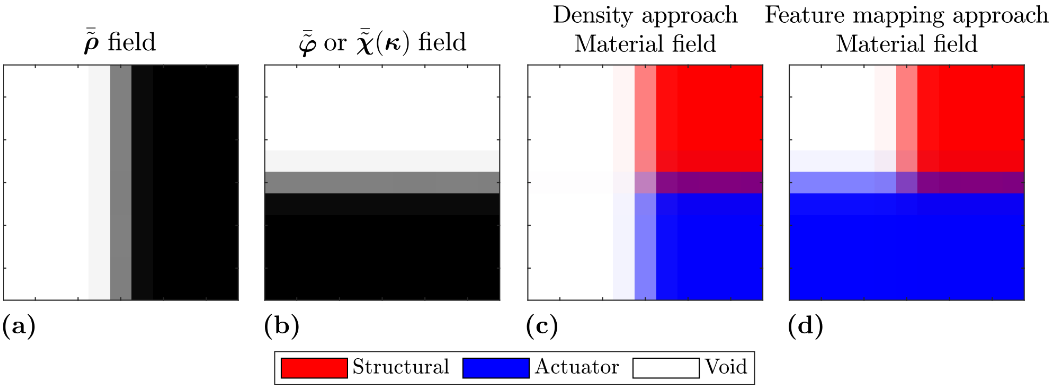

Figure 3. Illustration of the two density fields and two material fields. **(a)** and **(b)** show the density fields. **(c)** show how the material model is realized for the density approach. **(d)** show how the material model is realized for the feature mapping approach, notice how actuator material is dominating the material field when realizing the material model. As seen in **(c)** and **(d)** red material will define structural material, while blue material will define actuating material.

$$\mathcal{F}_1(\bar{\tilde{\rho}}, \bar{\tilde{\chi}}(\boldsymbol{\kappa})) = \sum_e \frac{V_e \bar{\tilde{\rho}}_e (1 - \bar{\tilde{\chi}}_e(\boldsymbol{\kappa}))}{V}, \qquad \mathcal{F}_2(\bar{\tilde{\chi}}(\boldsymbol{\kappa})) = \sum_e \frac{V_e \bar{\tilde{\chi}}_e(\boldsymbol{\kappa})}{V}. \tag{20}$$

The material property interpolation in (10) and (11) must be modified for the feature mapping approach. We proposed to extend (10) and (11) for a strict geometric feature representation as

$$G(\bar{\tilde{\rho}}_e, \bar{\tilde{\chi}}_e(\boldsymbol{\kappa})) = \left(\bar{\tilde{\rho}}_e^p - \left(\bar{\tilde{\rho}}_e^p - 1\right)\bar{\tilde{\chi}}_e(\boldsymbol{\kappa})^p\right)\Phi_G(\bar{\tilde{\chi}}_e(\boldsymbol{\kappa})), \tag{21}$$

$$K(\bar{\tilde{\rho}}_e, \bar{\tilde{\chi}}_e(\boldsymbol{\kappa})) = \left(\bar{\tilde{\rho}}_e^p - \left(\bar{\tilde{\rho}}_e^p - 1\right)\bar{\tilde{\chi}}_e(\boldsymbol{\kappa})^p\right)\Phi_K(\bar{\tilde{\chi}}_e(\boldsymbol{\kappa})). \tag{22}$$

The thermal expansion coefficient interpolation is the same as for the density approach; (12). An illustration of the two parameterization approaches is seen in Fig. 3, where it is seen how the two design fields are realized and how they are combined for the physical material field. Noticed for the feature mapping approach, how the feature mapped density field is dominating the material density field. As is defined in Fig. 3, *red material* will be defined as a structural material, while *blue material* will be defined as an actuating material, for any further figures of material fields.

3.3. Sensitivity Analysis

We use the adjoint method [19] to calculate the sensitivities of a function, f, which denotes either objective or constraint functions. The sensitivities of f are found though

$$\frac{\partial f\left(\bar{\tilde{\xi}}\right)}{\partial \bar{\tilde{\xi}}} = \frac{\partial f\left(\bar{\tilde{\xi}}\right)}{\partial \bar{\tilde{\xi}}} + \boldsymbol{\lambda}^\top \left(\frac{\partial \mathbf{f}\left(\bar{\tilde{\xi}}\right)}{\partial \bar{\tilde{\xi}}} - \frac{\partial \mathbf{K}\left(\bar{\tilde{\xi}}\right)}{\partial \bar{\tilde{\xi}}}\mathbf{u}\left(\bar{\tilde{\xi}}\right)\right), \tag{23}$$

where $\boldsymbol{\lambda}$ is the adjoint vector obtained from

$$\mathbf{K}\boldsymbol{\lambda} = \nabla_{\mathbf{u}} f\left(\bar{\tilde{\xi}}\right). \tag{24}$$

The chain rule is applied to obtain the sensitivities of f with respect to the design variables [21]

$$\frac{\partial f}{\partial \xi_e} = \sum_{i \in \mathbb{N}_e} \frac{\partial f}{\partial \bar{\tilde{\xi}}_i} \frac{\partial \bar{\tilde{\xi}}_i}{\partial \tilde{\xi}_i} \frac{\partial \tilde{\xi}_i}{\partial \xi_e}. \tag{25}$$

Similar for the feature mapped density field, the chain rule is applied to find the sensitives regarding the feature mapping design variables $\boldsymbol{\kappa}$.

3.4. Numerical Implementation

The topology optimization problem is implemented in a parallel 3D unstructured topology optimization framework by Träff *et al.* [26] based on work by Aage and Lazarov [27] utilizing the numerical library PETSc [28]. The finite element system is solved with a multigrid preconditioned Krylov method. The optimization problem is solved with the iterative optimization scheme, MMA [29].
Move limit for $\boldsymbol{\rho}$ and $\boldsymbol{\varphi}$ is set to 0.05, while move limits for $\boldsymbol{\kappa}$ is set to 0.05 for translation and volumetric expansion of the feature and 0.002 for rotation. A continuation approach is employed for the projection parameter β, updated by $\beta = 1.1\beta$ every 40th iteration with an upper limit of 64. For the feature mapping approach, β_2 is fixed to 10, furthermore, the β continuations approach is only started after 300 iterations. For the phase interpolation, we set $\Psi = 0$ for the density approach, however, as we want little penalization on the actuator strength in the feature mapping approach, $\Psi = 1$ is chosen.

4. Examples

This section aims to demonstrate and investigate how the proposed topology optimization method is applied to realize a large-scale 3D morphing wing structure via morphing trailing edge section design.
The trailing edge section was meshed using Cubit [30] with approximate element size of 0.5[mm], resulting in approximately 70 million elements and 210 million degrees of freedom. The mesh can not be illustrated fully here due to the small element size compared to the size of the geometry. Instead, a close-up of the results is presented in Fig. 4, where the mesh resolution is shown.
A filter radius $r_{\min} = 15[\text{mm}]$ is set on both density fields. 264 equally distributed target nodes are used to describe the morphing shape. We only prescribe the morphing displacement error in the vertical direction $(\bar{y})$, as the skin is relatively stiff. The upper bound values for the volume fraction and morphing constraints are listed in Tab. 2.

Table 2. Upper bound values for the constraints.

V_1^* [%]	V_2^* [%]	$\mathcal{E}^*$ [%]
5	1	2.5

The optimization has been run in the DTU Sophia cluster with 800 cores. The density approach result is obtained after 750 iterations, while the feature mapping approach is obtained after 1900 iterations, as the feature mapping approach is slow to converge. Each iteration takes on average 4-5 minutes.

Table 3. Initial normalized $(')$ design variables for the feature mapping approach.

x_0'	y_0'	z_0'	θ_1'	θ_2'	r'	l'
0.50	0.65	0.00	143/256	144/256	0.5	0.8

In the density approach, the design domains are initialized with a constant value that satisfies the volume constantdomains, according to (9). In the feature mapping approach, the actuator is initialized with the normalized $(')$ design variables listed in Tab. 3 (based on preliminary results obtained from the density approach). The initial design is seen in appendix A in Fig. 1.

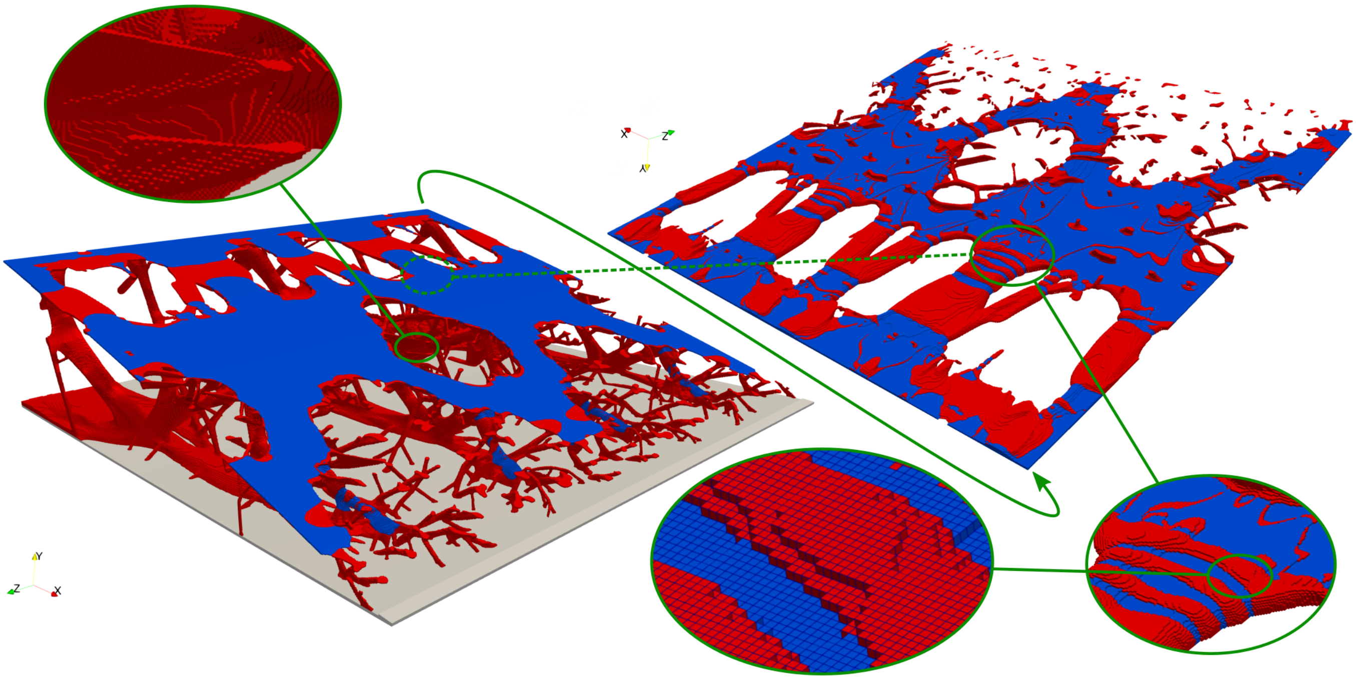

Figure 4. Isometric view of the resulting topology from the density approach with one design domain. The skin on the top side is removed for viewing the internal structure. The field is realized with a threshold value of 0.5. On the right side of the figure, a slice of the bottom side of the actuator portion is shown; notice the level of detail archived with the fine mesh discretization. In the top left corner, merging, plate-like, and truss structures are highlighted.

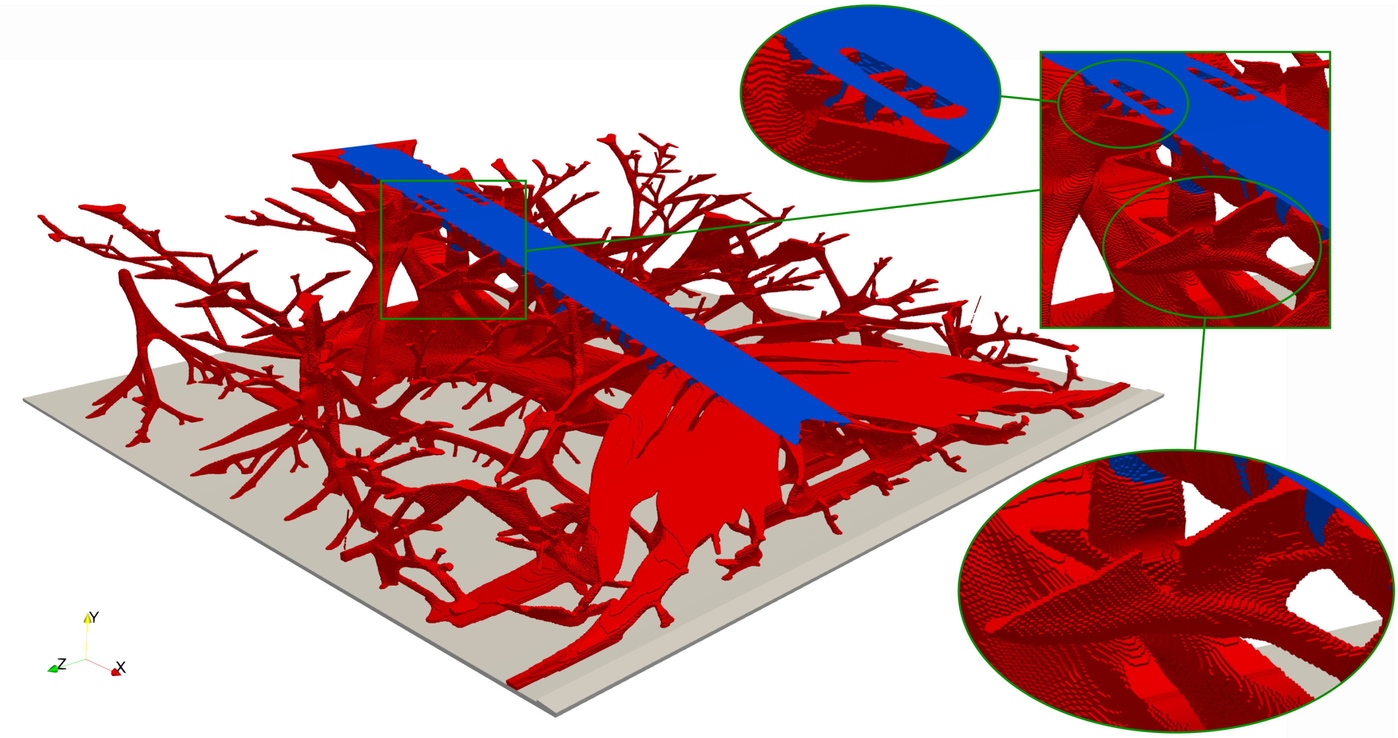

Figure 5. Isometric view of the optimized topology from the density approach with two design domains. The skin on the top side is removed for viewing the internal structure. The field is realized with a threshold value of 0.5. The top close-up shows structural material are forming a composite with actuating material for optimizing actuator capabilities. The bottom close-up shows truss structure merging into thin plate structure.

4.1. Density Approach

In the first result, both structural and actuating materials are freely distributed in the whole design domain, Ω. An overview of the optimized structure is shown in Fig. 4. It is seen that the structural material (red) has formed a very complex structure consisting of truss and plate-like components. The truss components branch out like tree branches to connect with the skin. The structures resembles gecko feet hair structures. The features are oriented to carry the load and have the bending stiffness required to obtain the constrained morphing shape. The actuating material (blue) has formed a thin plate-like structure at the tip-top of the trailing edge to provide maximum downwards bending moment. At the end of the trailing edge, a few truss actuators are seen. The close-up detail in Fig. 4 shows that the actuating material has formed a complex composite together with the structural material. The structural material forms rings around the actuating material to support the actuator, so both actuator force and stiffness are balanced, this resembles the effects of a weightlifter belt. Furthermore, a nearly periodic structure is observed, which provides a similar morphing shape along $\bar{z}$-direction.

From a manufacturing point of view, this result is too complex to realize. To simplify the actuating region, we now only allow the actuating material in Ω_2 (see Fig. 1). while structural material can be freely distributed in the whole domain. The optimized result is shown in Fig. 5. Similar to the previous case, the structural material forms truss and plate-like components. Differences are observed in how the structural material forms around the actuator, i.e., the middle of the domain. We see a stiff structure forming under the actuator and at the end of the actuator, which then branches out to provide the required mechanism to force the whole end of the trailing edge down.

In Fig. 6 and 7, the actuator portion of the structure is isolated and highlighted. Here we again see how a composite structure has formed between the actuator and structural material, such that the actuator provides the wanted force/displacement characteristics for the morphing. From Fig. 6 we see that defined compliant mechanisms with well-defined hinges are formed under the actuator to distribute the bending moment throughout the structure. In Fig. 7, the expansion for the actuator portion is shown, from 0% to 100%. Here the mechanism is seen to morph the structure.

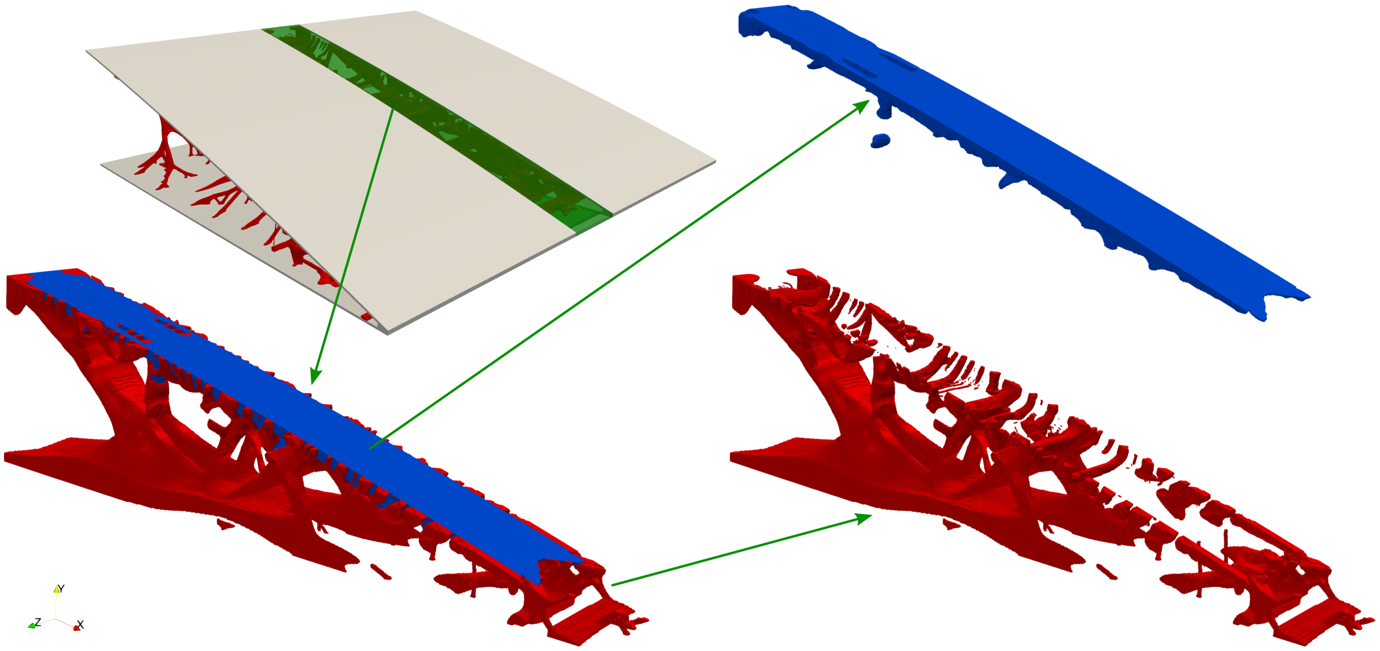

Figure 6. Isolation of actuator portion of resulting topology from the density approach with two design domains. The field is realized with a threshold value of 0.5. Notice how a very complex structural design has formed around actuating material.

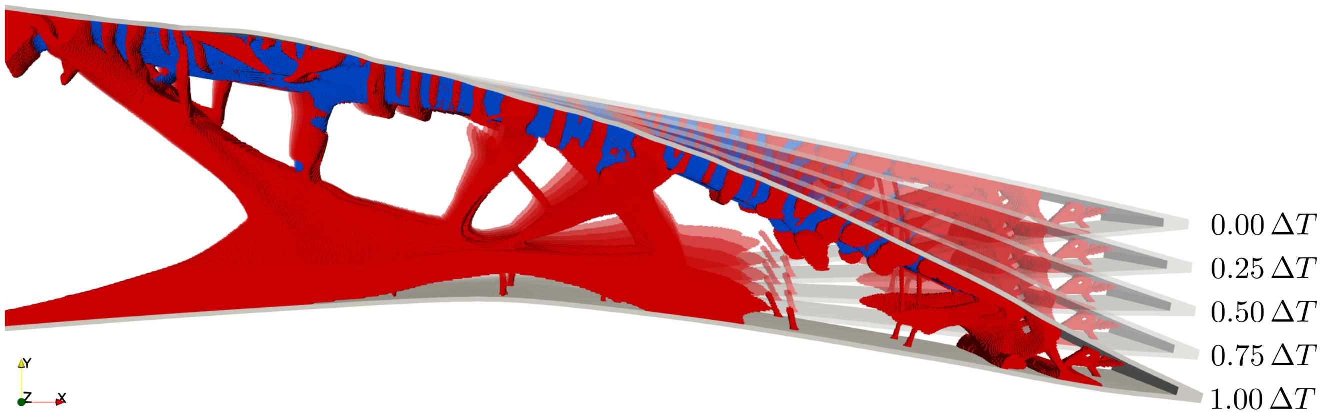

Figure 7. Demonstration of the morphing capabilities of the resulting topology from the density approach with two design domains. The field is realized with a threshold value of 0.5. The shown section is the same as highlighted in Fig. 6.

The actuating material seems to lump together in the two optimized designs, which makes the interpretations of a manufacturable design hard. For that reason, the feature mapping approach seems essential to explore.

4.2. Feature Mapping Approach

The final result is obtained using the feature mapping approach. An overview of the result is seen in Fig. 8. The result looks similar to the result obtained with the density approach for two domains. We again see how a stiff structure is formed under and at the end of the actuator to provide stiffness to the trailing edge section.

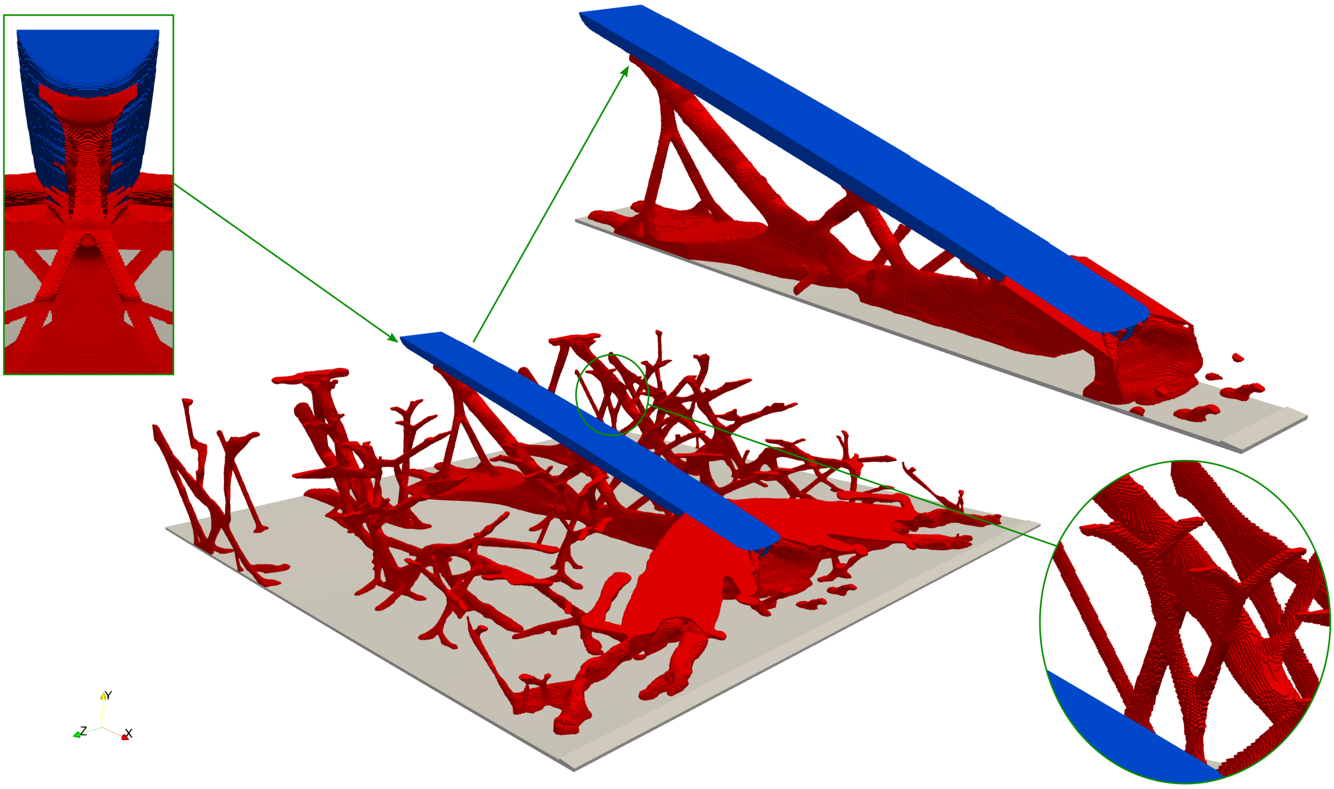

Figure 8. Isometric view of the resulting topology from the feature mapping approach. The skin on the top side is removed for viewing the internal structure. The field is realized with a threshold value of 0.5. The top-left close-up shows how the structural material is well connected to the actuation material. In the top-right corner, the actuator is isolated; notice how a compliant mechanism is formed under the actuator. The bottom-right close-up shows how a hierarchical branching structure is forming.

doi:10.20944/preprints202107.0051.v1

In Fig. 8, close-ups are highlighted; the close-up in the top-left corner shows how the structural material is forming cup-like features around the feature for connection between the actuator and structural material. The close-up in the lower-right shows how hierarchical branching structure is forming, as also seen on the density approach results.
Despite having constraints on the actuating material in the form of the feature mapping approach, it is evident that it is not enough to have strictly defined feature actuators as a cylinder. It is seen that the cylinder is moved halfway out of the skin. This makes sense from a mechanical perspective, as a more significant bending moment can be archived by moving more actuator material away from the structural mechanism.
Tab. 4 presents the structural compliance of the three optimized designs. While all designs satisfies the morphing constraint, it is seen that the compliance value of the structure with one design domain is lowest as expected due to the increased design freedom. When we constrain the density approach to two domains, the compliance value increases by 32% and 88% when using the feature mapping approach, as the structures have consciously less design freedom.

Table 4. Resulting compliance values from the three presented designs.

	Density approach (one domain)	Density approach (two domains)	Feature mapping approach
$\mathcal{C}$ [J]	$1.633 \cdot 10^{-5}$	$2.151 \cdot 10^{-5}$	$3.075 \cdot 10^{-5}$

It must be noted as pointed out by [24] that feature mapping problems are hard and tend to get stuck in local minimums. This observation holds also in this design problem as convergence of the problem is hard. Meanwhile, the structural material volume fraction constraint become inactive with a value of -0.019 while the actuating material volume fraction constraint is slightly violated with a value of 0.0034. This indicates that the actuator is not strong enough due to the geometric restriction in the feature mapping approach so that more structural material can be used.
Fig. 9 presents the deformed structure of the density approach with two domains (Fig. 9a) and the feature mapping approach (Fig. 9b). It is seen that the skin has a small uneven section in both designs and bends a bit upwards near the corners at the end trailing edge. These minor defects are expected when the morphing displacement error is constrained to an aggregated 2.5% error. Either lowering the error or increasing the p-value in the p-mean could mitigate this.

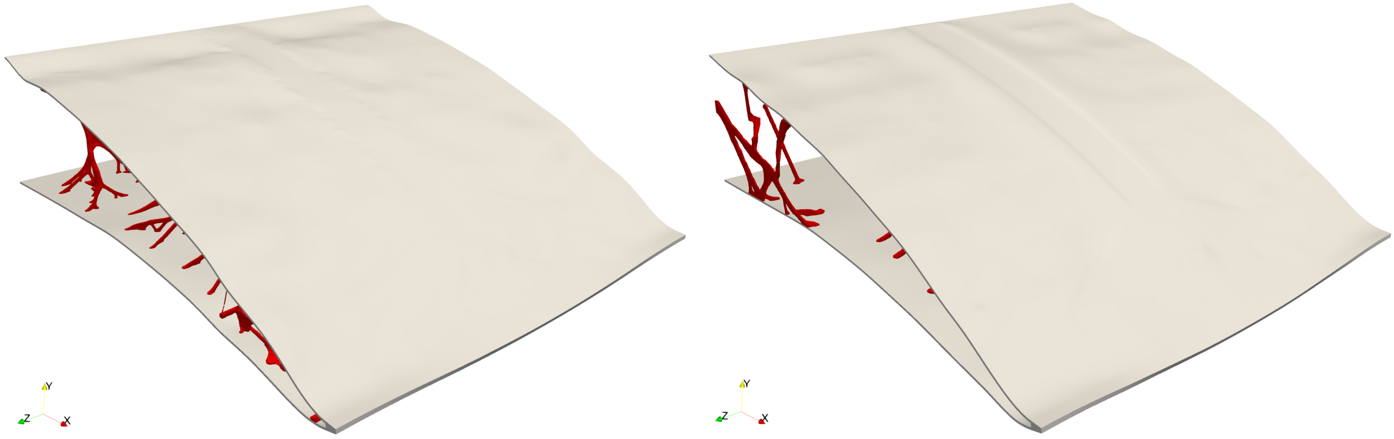

(a) **(b)**

Figure 9. Deformation fields of **(a)**: Density approach with two design domains. **(b)**: Feature mapping. Small defects in the skin are seen as a result of the morphing displacement error.

5. Discussion

In the reviewed literature, no true 3D model are presented; both Kambayashi *et al.* [9] and De Gaspari [12] present 2.5D results, where they performed optimization on 2D ribs that is connected to a 3D wing section. Our results cannot compared to theirs as they solve different problems and apply external loading to drive their model. However, the work presented here shows the possibility of morphing model structures in 3D and that the result may give an alternative wing structure, compared to the traditional one consisting of ribs, as proposed by Dimino *et al.* [31].

Furthermore, with the additions of actuator design formulation, it is possible to design a complex 3D mechanisms to achieve desired morphing shape while considering actuation. The optimized design from the feature mapping approach is easier to interpreter into a manufacturable object, which makes the method very versatile.

It was seen that the convergence in the feature mapping approach was very slow compared to the density approach. This is a drawback when using feature mapping approach, as this method is very sensitive to change. For this reason, a very low move limit was allowed for the design variables. Simultaneously, feature mapping is prone to local minimum issues that a low move limit does not help with.

The structural skin is an important component of a morphing trailing edge, as it is transferring external loading into the structure while it must remain smooth. In the presented work, the skin model was included as a passive component. One could imagine that if the skin was an active design domain, included in the modeling as done in [13], a better result could be obtained. Here the skin could be modeled as a shell structure.

6. Conclusions

This paper proposes a new approach to simultaneously optimize mechanism and actuator design for morphing structures using the topology optimization method. The morphing is achieved by constraining an error between actual and target shapes. Compliance minimization is utilized to ensure structural stiffness with respect to aerodynamic loading. Material properties are interpolated using a three-material model. The optimization problem of large-scale 3D morphing wings has been solved in an efficient parallel framework with an unstructured grid.

Both the density and feature mapping approaches are employed to design morphing trailing edge sections. Numerical results show that composite actuators have been formed to provide sufficient structural stiffness and actuating force in all the optimized designs. All three optimized designs show more unconventional design configurations and indicate that a 2D rib design may be inferior to a 3D design from pure mechanical observation. The feature mapping approach provides the simplest actuator geometry while the restriction on the actuator geometry leads to a most compliant design due to limited actuating force.

The presented method and examples have been applied for a very academic analysis for a 3D design domain and may serve as a baseline for further work and extensions. Nevertheless, we see this works as the first step towards systematic design of weight-efficient airplane morphing wing structures. The following points will be taken into accounts in future work, 1) Consider more in-depth analysis and optimization of the 3D trailing edge section for different load cases, multi-objectives, and different morphing targets; 2) Consider anisotropic forces via actuating material with anisotropic thermal expansion coefficients; 3) Include skin design in the optimization as seen in [13]. 4) Including geometrical non-linearity and manufacturing constants to obtain a more realistic design.

Author Contributions: Peter Dørffler Ladegaard Jensen: Methodology, Software, Formal analysis, Writing - review editing, Visualization. **Fengwen Wang**: Methodology, Conceptualization, Resources, Writing - review editing. **Ignazio Dimino**: Resources, Writing - review editing. **Ole Sigmund**: Methodology, Conceptualization, Resources, Writing - review editing.

Acknowledgments: The authors gratefully acknowledge the financial support of the Villum Foundation through the Villum Investigator project InnoTop.

Conflicts of Interest: The authors declare no conflict of interest.

Appendix A Feature Mapping Starting Guess

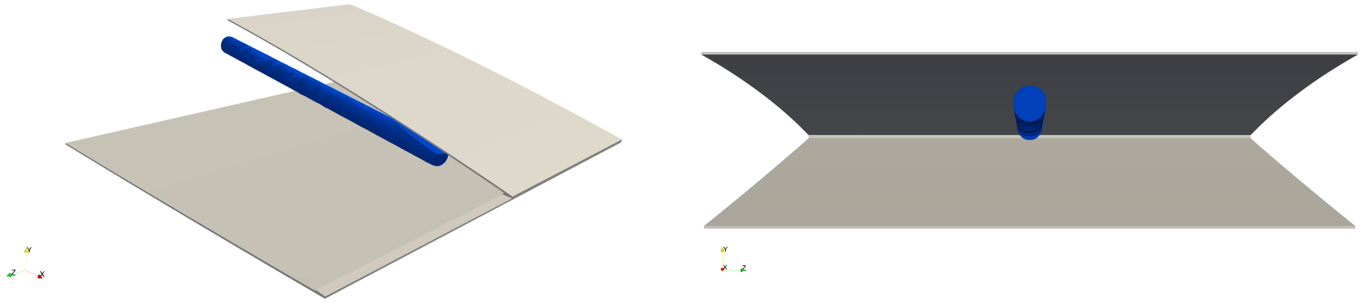

(a) **(b)**

Figure 1. Initial placement of feature for the feature mapping approach. **(a)**: Isometric view. **(b)**: Back view.

References

1. Holle, A.A. Plane and the Like for Aeroplanes. *United States Patent N.1225711* **1917**.
2. Parker, F.H. The Parker variable camber wing, Report No. 77. *National Advisory Committee for Aeronautics (NACA)* **1920**.
3. Bendsøe, M.P.; Kikuchi, N. Generating optimal topologies in structural design using a homogenization method. *Computer Methods in Applied Mechanics and Engineering* **1988**, *71*, 197–224. doi:10.1016/0045-7825(88)90086-2.
4. Bendsøe, M.P. *Optimization of Structural Topology, Shape, and Material*; Springer Berlin Heidelberg: Berlin, Heidelberg, 1995. doi:10.1007/978-3-662-03115-5.
5. Sigmund, O. On the Design of Compliant Mechanisms Using Topology Optimization. *Mechanics of Structures and Machines* **1997**, *25*, 493–524. doi:10.1080/08905459708945415.
6. Sigmund, O. Systematic Design of Micro and Macro Systems. In *IUTAM-IASS Symposium on Deployable Structures, Theory and Applications*; Springer, Dordrecht, 2000; Vol. 80, pp. 373–382. doi:10.1007/978-94-015-9514-8_39.
7. Sigmund, O. Design of multiphysics actuators using topology optimization – Part I: One-material structures. *Computer Methods in Applied Mechanics and Engineering* **2001**, *190*, 6577–6604. doi:10.1016/S0045-7825(01)00251-1.
8. Sigmund, O. Design of multiphysics actuators using topology optimization – Part II: Two-material structures. *Computer Methods in Applied Mechanics and Engineering* **2001**, *190*, 6605–6627. doi:10.1016/S0045-7825(01)00252-3.
9. Kambayashi, K.; Kogiso, N.; Yamada, T.; Izui, K.; Nishiwaki, S.; Tamayama, M. Multiobjective Topology Optimization for a Multi-layered Morphing Flap Considering Multiple Flight Conditions. *Transactions of the Japan Society for Aeronautical and Space Sciences* **2020**, *63*, 90–100. doi:10.2322/tjsass.63.90.
10. Tong, X.; Ge, W.; Yuan, Z.; Gao, D.; Gao, X. Integrated design of topology and material for composite morphing trailing edge based compliant mechanism. *Chinese Journal of Aeronautics* **2021**, *34*, 331–340. doi:10.1016/j.cja.2020.07.041.
11. Zhang, Z.; Ge, W.; Zhang, Y.; Zhou, R.; Dong, H.; Zhang, Y. Design of Morphing Wing Leading Edge with Compliant Mechanism. In *Lecture Notes in Computer Science (including subseries Lecture Notes in Artificial Intelligence and Lecture Notes in Bioinformatics)*; Springer International Publishing, 2019; Vol. 11740 LNAI, pp. 382–392. doi:10.1007/978-3-030-27526-6_33.
12. De Gaspari, A. Multiobjective Optimization for the Aero-Structural Design of Adaptive Compliant Wing Devices. *Applied Sciences* **2020**, *10*, 6380. doi:10.3390/app10186380.
13. Gomes, P.; Palacios, R. Aerodynamic Driven Multidisciplinary Topology Optimization of Compliant Airfoils. AIAA Scitech 2020 Forum; American Institute of Aeronautics and Astronautics: Reston, Virginia, 2020; Vol. 1 PartF, pp. 2117–2130. doi:10.2514/6.2020-0894.
14. Gu, X.; Yanf, K.; Wu, M.; Zhang, Y.; Zhu, J.; Zhang, W. Integrated optimization design of smart morphing wing for accurate shape control. *Chinese Journal of Aeronautics* **2021**, *34*, 135–147. doi:10.1016/j.cja.2020.08.048.
15. Arena, M.; Amoroso, F.; Pecora, R.; Amendola, G.; Dimino, I.; Concilio, A. Numerical and experimental validation of a full scale servo-actuated morphing aileron model. *Smart Materials and Structures* **2018**, *27*, 105034. doi:10.1088/1361-665x/aad7d9.

16. Vecchia, P.; Corcione, S.; Pecora, R.; Nicolosi, F.; Dimino, I.; Concilio, A. Design and integration sensitivity of a morphing trailing edge on a reference airfoil: The effect on high-altitude long-endurance aircraft performance. *Journal of Intelligent Material Systems and Structures* **2017**, *28*, 2933–2946. doi:10.1177/1045389X17704521.
17. Mark Drela. XFOIL 6.97 **2020**.
18. Cook, R.D.; Malkus, D.S.; Plesha, M.E.; Witt, R.J. *Concepts and Applications of Finite Element Analysis (4nd Edition)*; John Wiley & Sons, Incorporated, 2001.
19. Bendsøe, M.P.; Sigmund, O. *Topology Optimization*; Springer Berlin Heidelberg: Berlin, Heidelberg, 2004; p. 381. doi:10.1007/978-3-662-05086-6.
20. Bourdin, B. Filters in topology optimization. *International Journal for Numerical Methods in Engineering* **2001**, *50*, 2143–2158. doi:10.1002/nme.116.
21. Wang, F.; Lazarov, B.S.; Sigmund, O. On projection methods, convergence and robust formulations in topology optimization. *Structural and Multidisciplinary Optimization* **2011**, *43*, 767–784. doi:10.1007/s00158-010-0602-y.
22. Lazarov, B.S.; Sigmund, O. Filters in topology optimization based on Helmholtz-type differential equations. *International Journal for Numerical Methods in Engineering* **2011**, *86*, 765–781. doi:10.1002/nme.3072.
23. Norato, J.; Haber, R.; Tortorelli, D.; Bendsøe, M.P. A geometry projection method for shape optimization. *International Journal for Numerical Methods in Engineering* **2004**, *60*, 2289–2312. doi:10.1002/nme.1044.
24. Wein, F.; Dunning, P.D.; Norato, J.A. A review on feature-mapping methods for structural optimization. *Structural and Multidisciplinary Optimization* **2020**, *62*, 1597–1638. doi:10.1007/s00158-020-02649-6.
25. Wang, F. Systematic design of 3D auxetic lattice materials with programmable Poisson's ratio for finite strains. *Journal of the Mechanics and Physics of Solids* **2018**, *114*, 303–318. doi:10.1016/j.jmps.2018.01.013.
26. Träff, E.A.; Sigmund, O.; Aage, N. Topology optimization of ultra high resolution shell structures. *Thin-Walled Structures* **2021**, *160*, 107349. doi:10.1016/j.tws.2020.107349.
27. Aage, N.; Lazarov, B.S. Parallel framework for topology optimization using the method of moving asymptotes. *Structural and Multidisciplinary Optimization* **2013**, *47*, 493–505. doi:10.1007/s00158-012-0869-2.
28. Balay, S.; Abhyankar, S.; Adams, M.; Brown, J.; Brune, P.; Buschelman, K.; Dalcin, L.; Dener, A.; Eijkhout, V.; Gropp, W.; Karpeyev, D.; Kaushik, D.; Knepley, M.; May, D.; McInnes, L.C.; Mills, R.; Munson, T.; Rupp, K.; Sanan, P.; Smith, B.; Zampini, S.; Zhang, H.; .; Zhang, H. *PETSc - Portable, Extensible Toolkit for Scientific Computation*. Argonne National Laboratory, revision 3.13 ed., 2020.
29. Svanberg, K. The method of moving asymptotes—a new method for structural optimization. *International Journal for Numerical Methods in Engineering* **1987**, *24*, 359–373. doi:10.1002/nme.1620240207.
30. Sandia. Cubit 13.2 user documentation **2019**.
31. Dimino, I.; Amendola, G.; Di Giampaolo, B.; Iannaccone, G.; Lerro, A. Preliminary design of an actuation system for a morphing winglet. 2017 8th International Conference on Mechanical and Aerospace Engineering (ICMAE), 2017, pp. 416–422. doi:10.1109/ICMAE.2017.8038683.